SIMULATING NEAR-FIELD EFFECTS IN HIGH-DENSITY OPTICAL-DISK DATA STORAGE

Plane-wave expansion methods for classical diffraction theory equations, coupled with the direct numerical solution of Maxwell's equations using local grid refinement and the finite-difference time-domain method, help us reliably simulate an optical system's macroscopic and subwavelength components.

Designing an optical data storage system involves both macroscopic components, such as lenses, filters, and polarizers, which are typically tens of thousands of wavelengths in size, as well as subwavelength-size data elements, gratings, near-field antennas, and microcavities. Research and development of new approaches for high-density optical-disk data storage often requires detailed simulation of the light-field interaction with subwavelength structures.

Optical disks based on current compact disk (CD) and digital versatile disk (DVD) technologies operate near the wavelength $\lambda = 650$ nanometers and have geometric features about 400 nm in size. The ever-increasing demand for higher capacity and more compact storage systems has led to a continuous decrease of the size and increased geometrical complexity of the subwavelength components.

We can numerically model propagation of the light field through many elements of the optical system using classical diffraction theory equations and plane-wave expansion solution methods. These global spectral transform methods, which use fast Fourier transforms, provide accurate and efficient solutions for such cases.[1,2] However, when the light field interacts with structures on scales comparable to the wavelength, the classical diffraction theory's assumptions, invoked to simplify the problem and allow for approximate solutions, are not applicable. For such cases, we seek numerical solutions of Maxwell's equations (in conjunction with the relevant constitutive relations) by approximating the continuous time and space derivatives via the appropriate difference operators.

Interfacing and combining the solution procedures applicable for different limiting cases lets us accurately simulate the complete optical-disk data-storage system. Simulating the entire system lets us compute optical system performance characteristics, which can also be measured in the experiment, making computations a more direct design tool.

1521-9615/03/$17.00 © 2003 IEEE
Copublished by the IEEE CS and the AIP

ARAMAIS R. ZAKHARIAN, JEROME V. MOLONEY, AND MASUD MANSURIPUR
University of Arizona

Finite-Difference Time-Domain Method

The finite-difference time-domain (FDTD) method discretizes Maxwell's equations by using a central difference operator in both the time and space variables.[3] The **E** and **H** fields are represented by their discrete values on the spatial grid and are advanced in time steps of Δt. We stagger the components of the vector fields **E** and **H** so that every

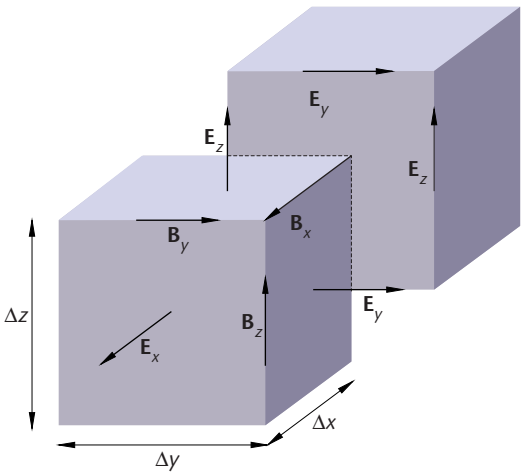

Figure 1. The unit cell of the finite-difference time-domain mesh. The field components are shifted by a half-pixel in various directions. The E and H field components are shifted so that each E field component normal to the cell face is surrounded by the circulation of the H field components defined on the cell edges.

component of the electric field is surrounded by the magnetic field's four circulating components, and vice versa (see Figure 1). Considering the integral form of Maxwell's curl equations motivates such a staggered grid. The contour integrals of **E**(**H**) along the cell's edges in Faraday's (Ampere's) law circulate around the corresponding magnetic (electric) field component at the cell face's center.

The FDTD algorithm solves Maxwell's equations in the time domain. Because the solution is time dependent, it allows pulses in time, which in turn means that the system response for many frequencies can be computed in a single simulation. Additionally, we can readily incorporate several commonly used material-dispersion models into the time-dependent formulation.[4] We can adequately model high-reflectivity metallic layers and metal-coated data elements in optical-disk data-storage problems with Debye, Drude, or Lorentz material-dispersion models, using either a linear recursive filter or auxiliary differential equation approaches.

Simulating the near-field interaction of the focused light beam with an optical data element on the disk surface usually requires a computational domain only a few wavelengths in size. Low-reflection boundary conditions developed for FDTD simulations, such as Mur's absorbing boundary and the perfectly matched layer (PML) boundary condition,[4] let us calculate the problems requiring open boundaries with a signal-to-noise ratio near the –50-db level. PML boundary conditions, combined with the total-field, scattered-field technique for the source-field distribution, allow accurate evaluation of the incident, reflected, and transmitted beams throughout the computational domain.

Although the FDTD method's numerical discretization does not introduce additional dissipation into the physical problem, it contributes to the numerical dispersion error. Consequently, in the second-order accurate FDTD scheme, the numerical phase velocities acquire $O(h^2)$ error. To reduce the resulting grid-dependent velocity anisotropy and the phase errors to 0.1 percent, approximately $N_{ppw} = 30$ points per wavelength are necessary.

Compared to spectral methods, these large N_{ppw} values, together with N_{ppw}^3 scaling of the memory and computation cost for 3D simulations, necessitate parallel implementation of the FDTD method. The explicit time update and short finite-difference stencil lead to a high degree of memory access locality, which enables good speedup for codes based on different parallel computing paradigms. For example, the measured performance on 32-node distributed-shared memory SGI Origin 3400 systems, using the message-passing interface[5] implementation, indicates 97 to 99 percent efficiency in speedup.

FDTD Local Grid Refinement

When simulating optical-disk data-storage components, the subwavelength geometric features' resolution is often the determining factor in choosing the cell size, rather than the number of points per wavelength. We desire geometry-adaptive grid refinement in such cases for efficiency. The basic FDTD method's structured, nonuniform, Cartesian grid is computationally efficient, but limited in its flexibility. In addition, the geometry represented on the Cartesian grid is approximated by a staircase pattern, unless we use a special update scheme at the material boundaries. To address these shortcomings, FDTD method generalizations were developed for the unstructured or curve–linear body fitted grids by using more flexible data structures and coordinate metric transformations of the equations.[4]

Nonconformal Cartesian grids retain efficiency of the basic FDTD algorithm on the structured grid, while still allowing solution or geometry-dependent grid refinement.[6–8] The grid consists of a hierarchy of nested rectangular regions (see Figure 2). At the refinement tree's root is a coarse grid covering the entire computational domain. Each successive level consists of a collection of rectangular regions with cell sizes refined by a fixed ratio (typically twice) and nested within their parent grids.

Such recursive refinement of the 3D computational domain can be efficient. For example, in problems of focused beam interaction with wavelength size structures, when the most refined region's size is 1/4 of the computational domain size and we use two refinement levels, an order of magnitude improvement in computation time can be obtained.

In addition to refining the spatial grid, we can also refine the time step at each grid level—the grids with cell size h doing half as many iterations as grids with cell size $h/2$. Inside each rectangular region, we apply the standard FDTD algorithm, while at the interfaces between the coarse and fine grids, we must use an interpolation in space and time to coordinate solutions at different levels. Due to the FDTD scheme's numerical dispersion, the fine grid's propagating modes at frequencies near and above the coarse grid's numerical cutoff frequency can have a reflection coefficient larger than unity. This leads to amplification of the high-frequency modes and results in the scheme's instability. To achieve stability, we use a high-order interpolation scheme at the boundary.[9]

The mesh refinement algorithm we describe can take advantage of several software frameworks (see the Berkeley Lab Adaptive Mesh Refinement at http://seesar.lbl.gov/amr/ and Paramesh at http://sdcd.gsfc.nasa.gov/RIB/repositories/inhouse_gsfc/Users _manual/amr.html) that implement the abstractions necessary for the recursive update, grid management, and parallelization of computations.

The FDTD-based space–time local mesh refinement retains a $O(h^2)$ convergence rate of the standard FDTD scheme but does not address the problem of the staircase approximation of the material interfaces that are not conformal to the grid lines. When optical data storage problems require us to solve Maxwell's equations in complex geometries and with a higher-order accuracy than currently possible with low-order methods, the discontinuous Galerkin (DG) spectral-element methods[10–12] offer a potential alternative. For problems with discontinuous material properties, these methods combine the flexibility of the unstructured grids widely used in low-order finite-element methods with the high-order convergence rates characteristic of global spectral methods. The DG spectral-element method offers two paths to convergence: reducing the element sizes (increasing the number of elements) or increasing the order of the polynomial approximations in each element.

Modeling Optical Data-Storage Components

We can apply the FDTD method in combination with Diffract,[1] a software package that models propagation of the light field through optical system, to model the interaction between a focused light beam and elements of the optical disk in the focal region. Masud Mansuripur, Aramais Zakharian, and Jerome Moloney provide details of the validation of the computation procedure and additional examples.[13]

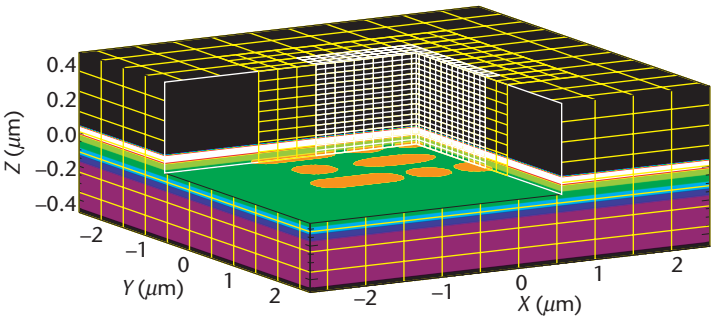

Figure 2. The 3D computational domain for simulating the interaction between a focused light beam and the marks on a multilayer data-storage device's surface. The grid is refined near the center, at the position of the focused beam.

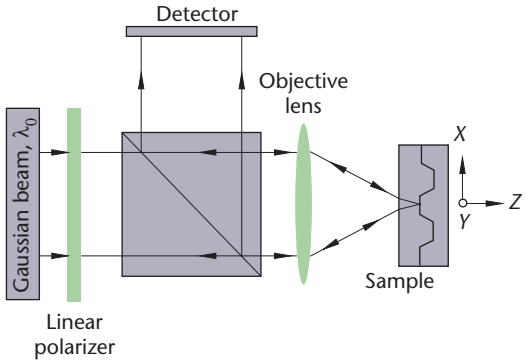

Figure 3. Schematic diagram of the simulated system setup. An aberration-free objective lens focuses a coherent, monochromatic beam of light.

Figure 3 shows a schematic of the numerical experiment setup, in which a coherent, monochromatic light beam (free-space wavelength = λ_0) is brought to focus by an aberration-free objective lens (numerical aperture NA = 0.6 and focal length f = 5,000 λ_0). The incident beam at the lens' entrance pupil is linearly polarized along x and is Gaussian with $1/e$ (amplitude) radius of 4,000 λ_0 truncated at the lens aperture (radius 3,000 λ_0). We can define the light's integrated intensity over the xy plane for the polarization's x and y components as

$$P_x = \int dx \int dy\, |E_x|^2, \qquad P_y = \int dx \int dy\, |E_y|^2. \qquad (1)$$

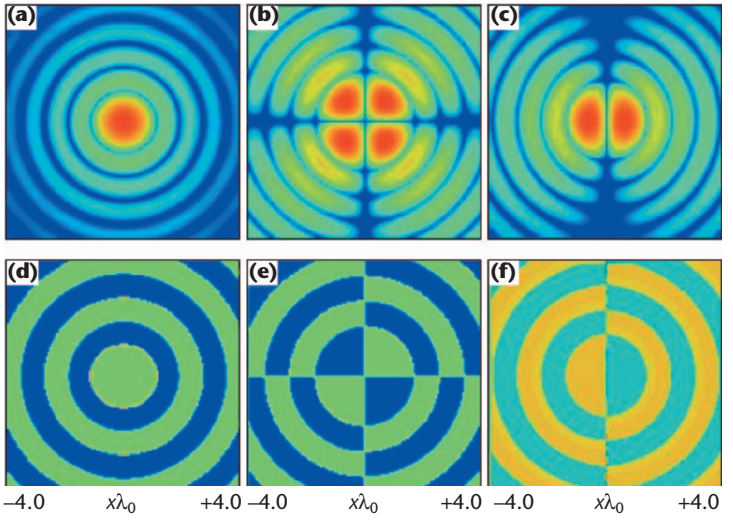

Figure 4. Computed plots of intensity and phase at the focal plane of the lens Figure 3 depicts. (a) – (c) Plots of log_intensity_4 and (d) – (f) phase at the focal plane. Left to right: *E*-field components along the *x*, *y*, and *z* axes.

The total integrated intensity at the lens' entrance pupil is $P_x = 1$ and $P_y = 0$.

Figure 4 shows computed plots of intensity (top) and phase (bottom) at the focal plane of the lens Figure 3 depicts. From left to right, these distributions represent the *E*-field components along the *x*, *y*, and *z* axes. At the focal plane, the peak intensities are in the ratio of $|E_x|^2 : |E_y|^2 : |E_z|^2 = 1{,}000 : 0.4 : 45$ and the fraction of optical energy carried by E_z is 8.3 percent of the total.

When the light is focused on the storage medium through the substrate, we assume (in the computation) the objective lens has been corrected for the aberrations the substrate caused, yielding an aberration-free focused spot in both cases of incidence through the substrate as well as direct incidence on the sample from the air side. We compute light-field propagation through the lens and into the sample up to the structure's surface using plane-wave expansion methods and the resulting distribution at the focal plane serves as an input to the FDTD solver.

We plotted the intensity and phase distributions in this article in an interval $x_{min} \le x \le x_{max}$ and $y_{min} \le y \le y_{max}$ of the *xy* plane by assigning the color red to the function's maximum value, blue to the minimum value, and the continuum of the white light spectrum to the values in between. The phase plots cover the range from –180° (blue) to 180° (red). The intensity distributions are first normalized to the function's peak value—for example, $I_{x\ peak} = \text{Max}(|E_x^2|)$—within the displayed interval. The normalized function's base 10 logarithm is then evaluated, and all pixel values below a certain level, say, $-\alpha$, are set equal to $-\alpha$. Displayed plots of log_intensity_α thus cover the range from $10^{-a} I_{peak}$ (blue) to I_{peak} (red).

In the first example, we compute reflection from convex and concave pits, similar to those found on a CD or DVD's plastic substrate. The substrate is embossed with a sphero-cylidrical pit with a 500-nm length along *x*, a 300-nm width along *y*, and a 100-nm depth along *z* (see Figure 5). The substrate's index is $n = 1.5$, and the metal film's thickness and complex index are $d = 50$ nm and $n + ik = 2.0 + 7.0\,i$. In the FDTD simulations, the incident wavelength was $\lambda_0 = 650$ nm, the mesh size was $L_x = L_y = 12\,\lambda_0$, and the metal film's front facet was at $\Delta z = 280$ nm beyond the focal plane.

In the case of a convex pit, the focused spot illuminates the sample directly so the light is incident on the pit from the air side—that is, $n_1 = 1.5$, $n_2 = 1$ in

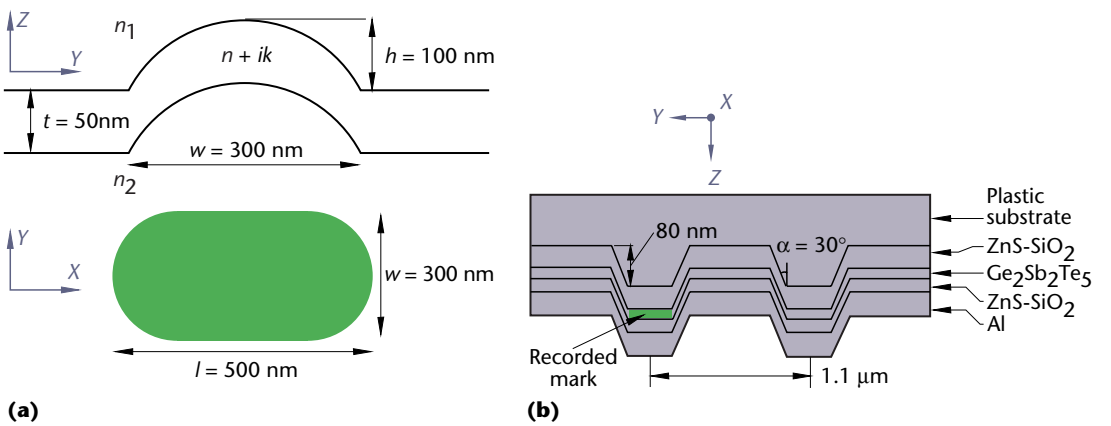

Figure 5. A plastic substrate as it would be found on a CD or DVD. (a) *xy* and *yz* cross sections of the sphero-cylindrical pit. (b) *yz* cross section of the multilayer grooved optical-disk structure. The $Ge_2Sb_2Te_5$ phase change layer has thickness $d = 35$ nm and index $n + ik = 4.6 + 4.2\,i$ in crystalline state. The ZnS-SiO_2 ($n = 2.1$) layers have thickness $d = 70$ nm on the top and $d = 35$ nm on the bottom. The structure is coated with a 70-nm thick aluminum film ($n + ik = 2.0 + 7.0\,i$).

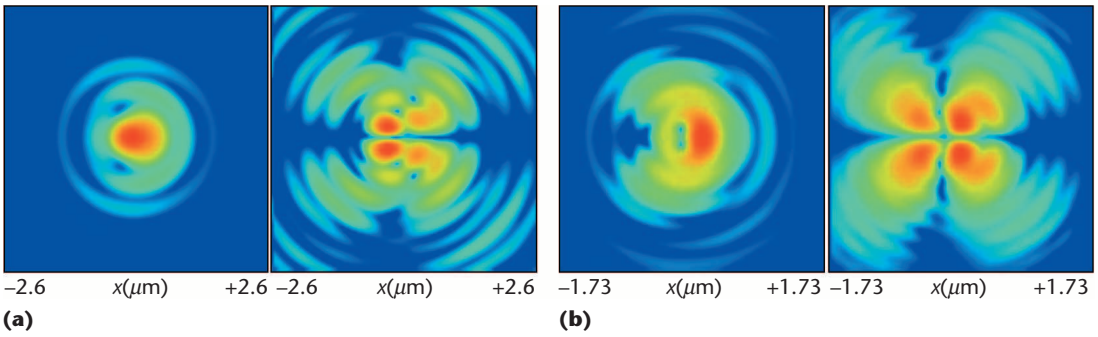

Figure 6. Plots of reflected log_intensity_3, of E_x and E_y components, from the (a) convex and (b) concave pits.

Figure 5, and the incidence medium is n_2. Figure 6a shows computed plots of reflected log_intensity_3 for E_x and E_y field components, in the case of a pit whose center was displaced by $\Delta x = -250$ nm from the focused spot's center. The computed integrated intensities for the x and y components of polarization in this example are $P_x = 0.82$ and $P_y = 0.0025$.

In a CD or DVD, the laser does not shine directly on the pit. Rather, the beam arrives through a plastic parallel plate cover, so with $n_1 = 1.5$, $n_2 = 1$ in Figure 5, the incidence medium is n_1. We simulate this case of a substrate-side incidence (concave pits) using the mesh size $L_x = L_y = 8\ \lambda_0$ and the same pit parameters as for the convex pit. The integrated intensities for the x and y components of polarization in this case were $P_x = 0.77$, $P_y = 0.022$, and Figure 6b shows the field distributions. Comparing $|E_x|^2$ distributions reveals that, whereas the convex pit tends to concentrate the incoming rays toward the pit center, the concave pit disperses these rays away from the center.

To obtain the read-out signals from the concave pit's laser-beam scan, the reflected light is propagated back through the substrate and out to the lens. At the collimating lens' exit pupil, the photodetector records the signal. Figure 7 shows a signal computed from a scan of a 500-nm-long concave pit. The signal's magnitude increases by about a factor of two as the beam center moves from the pit center beyond its edge.

In the second example, we simulate reflection of a focused light beam from the grooves and the recorded marks (see Figure 5a) analogous to those used in optical rewritable data storage media. An initial Gaussian light beam at the wavelength $\lambda_0 = 650$ nm is focused on the grooves through a plastic cover with refractive index $n = 1.5$. A phase change layer of $Ge_2Sb_2Te_5$ in a crystalline state is clad with conformal layers of ZnS-SO_2 and an aluminum layer on the bottom. The groove duty cycle is 40 percent, the depth is 80 nm, and deviation of the angle of groove from the normal is 30°.

Figure 8 shows the reflected light's computed

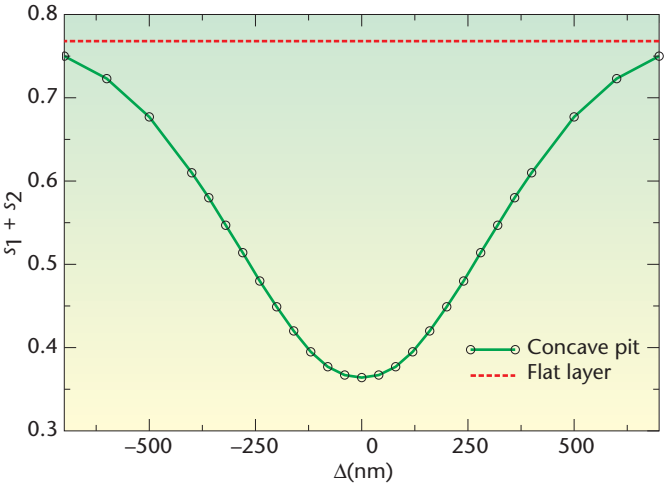

Figure 7. Total integrated intensity, $s_1 + s_2$, received at the detector, vs. offset, Δ, of the beam center from the pit center. The dashed line corresponds to the signal detected from the flat layer.

near-field intensities and phase distributions, when the incident beam is focused on the center of the groove (top, $P_x = 0.31$, $P_y = 0.0021$) and when the focused spot is shifted toward the edge of the groove (bottom, $P_x = 0.29$, $P_y = 0.0014$).

By propagating the light back through the system, we obtain the corresponding intensity profile at the collimating lens' exit pupil (see Figure 9), which gives a baseball-type pattern due to the reflected field's different diffraction orders. The distribution's nonuniformity on small spatial scales is because of the finite size of the FDTD computational domain size, $L_x = L_y = 20\lambda_0$, which truncates the incident beam distribution. With a split detector system aligned along the grooves, we can evaluate a push–pull tracking signal by scanning the incident beam across the groove. Figure 10 shows the signals s_1 and s_2, received by each detector, and the resulting push–pull signal $S = (s_1 - s_2)/(s_1 + s_2)$. For positive values of Δ, S reaches its minimum at $\Delta = 200$ nm (groove edge) and goes through

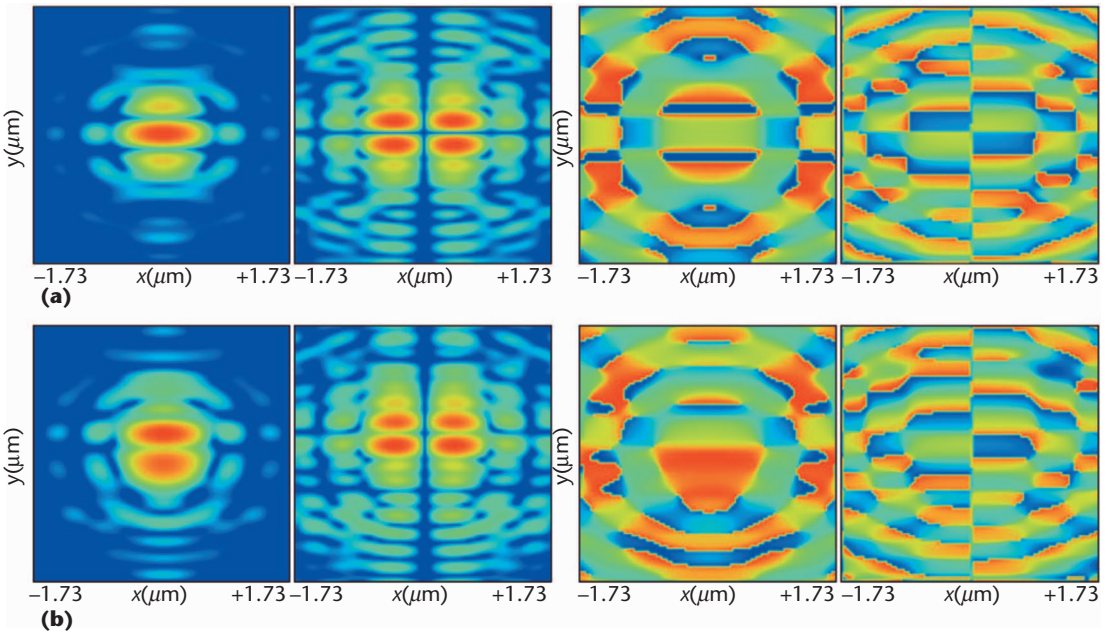

Figure 8. Plots of reflected log_intensity_3 and phase. The grooves are shifted from the focused spot center along the *y* axis by (a) Δ = 0 and (b) Δ = 250 nm.

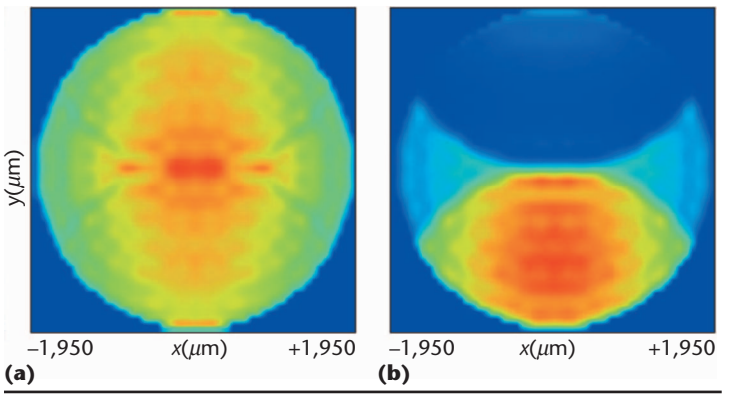

Figure 9. Intensity distribution of the E_x field component at the lens' exit pupil. We show reflected fields for the case of an incident beam (a) centered on the groove and incident beam center (b) shifted by Δ = 250 nm. The shift is in the vertical direction (along the *y* axis) away from the groove center and toward the groove edge.

the zero when the beam is centered on the groove (Δ = 0) or on the land (Δ = 550 nm).

Figure 11 shows plots of the computed intensity distribution for the groove sample containing a recorded amorphous mark. The circular mark's refractive index is $n + ik = 4.4 + 2.1\,i$ (amorphous state of $Ge_2Sb_2Te_5$), and its diameter is 360 nm. The relatively large groove depth, equal to 80 nm, and the thickness of the phase-change layer, 35 nm, that we used in this simulation lead to only 3.5 percent contrast in the signal recorded at the detector between the cases of the beam centered on and off the mark.

Using the plane-wave expansion methods and classical diffraction theory for the macroscopic elements of the optical system and direct solution of the electromagnetics equations for the wavelength-sized components enables accurate design of the optical data-storage systems. FDTD methods based on the local grid refinement approach allow improved computational efficiency for simulations involving light interaction with optical-disk elements on the subwavelength scales. To make these methods more robust when dealing with complicated geometric shapes that are not aligned with the coordinate grid lines, we must develop field-matching conditions that can accurately represent material interfaces across the cut cell boundaries. Further work is also required to evaluate the method's stability for the geometries in which refined grid boundaries cross material interfaces or absorbing PML boundaries.

Another research direction is developing scalable parallel implementations of the algorithm because most of the practical problems require a parallel computing environment.

Acknowledgments

We are grateful to Moysey Brio and Colm Dineen for helpful discussions. The computer simulations in this article were performed by Diffract, a product of MM

Research, Tucson, Arizona, and by the FDTD program Sim3D_Max, a product of NLCSTR, Tucson, Arizona. This work has been supported in part by the US Air Force Office of Scientific Research (F49620-02-1-0380).

References

1. M. Mansuripur, *The Physical Principles of Magneto-Optical Recording,* Cambridge Univ. Press, 1995.
2. M. Mansuripur, *Classical Optics and Its Applications,* Cambridge Univ. Press, 2002.
3. K.S. Yee, "Numerical Solution of Initial Boundary Value Problems Involving Maxwell's Equations in Isotropic Media," *IEEE Trans. Antennas and Prop.*, vol. 14, May 1966, pp. 302–307.
4. A. Taflove and S.C. Hagness, *Computational Electrodynamics,* Artech House, 2000.
5. W. Gropp, E. Lusk, and A. Skjellum, *Using MPI: Portable Parallel Programming Using Message Passing Interface,* MIT Press, 1999.
6. P. Thoma and T. Weiland, "A Consistent Subgridding Scheme for the Finite Difference Time Domain Method," *Int'l J. Numerical Modeling,* vol. 9, no. 5, 1996, pp. 359–374.
7. M. Okoniewski, E. Okoniewski, and M.A. Stuchly, "Three-Dimensional Subgridding Algorithm for FDTD," *IEEE Trans. Antennas and Propagation,* vol. 45, no. 3, 1997, pp. 422–429.
8. P. Monk, "Sub-Gridding FDTD Schemes," *Applied Computational Electromagnetics Soc. J.*, vol. 11, no. 1, 1996, pp. 37–46.
9. A.R. Zakharian, M. Brio, and J.V. Moloney, "FDTD Based Local Mesh Refinement Method for Maxwell's Equations in Two Space Dimensions," submitted to *SIAM J. Scientific Computing,* 2003.
10. D. Kapriva, S.L. Woodruff, and M.Y Hussaini, "Discontinuous Spectral Element Approximation of Maxwell's Equations," *Discontinuous Galerkin Methods: Theory, Computation and Applications,* Lecture Notes in Computational Science and Eng., vol. 11, B. Cockburn, G.E. Karniadakis, and C.W. Shu, eds., Springer-Verlag, 2000, pp. 355–362.
11. T. Warburton, "Application of the Discontinuous Galerkin Method to Maxwell's Equations Using Unstructured Polymorphic hp-Finite Elements," *Discontinuous Galerkin Methods: Theory, Computation and Applications,* Lecture Notes in Computational Science and Eng., vol. 11, B. Cockburn, G.E. Karniadakis, and C.W. Shu, eds., Springer-Verlag, 2000, pp. 451–458.
12. J.S. Hesthaven and T. Warburton, "Nodal High-Order Methods on Unstructured Grids. I. Time-Domain Solution of Maxwell's Equations," *J. Computational Physics,* vol. 181, no. 1, 2002 pp. 186–221.
13. M. Mansuripur, A.R. Zakharian, and J.V. Moloney, "Interaction of Light with Subwavelength Structures," *Optics and Photonics News,* vol. 14, Mar. 2003, pp. 56–61.

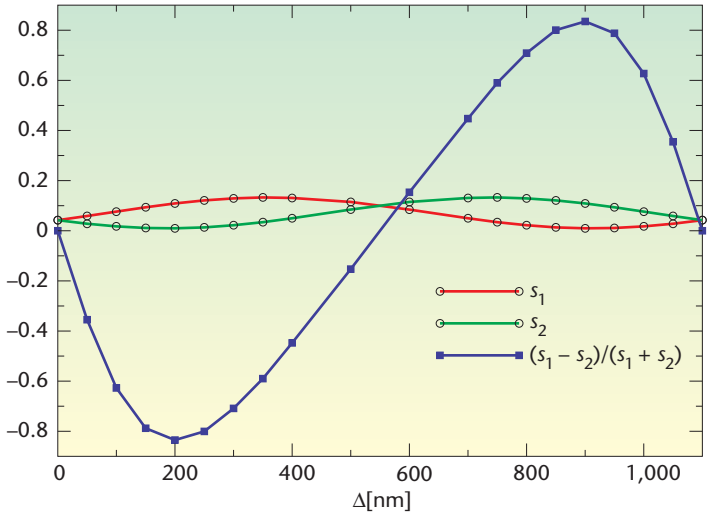

Figure 10. Intensities s_1 and s_2, recorded by each detector, and corresponding push–pull tracking signal versus offset, Δ, of the beam center from the groove center.

Aramais R. Zakharian is a postdoctoral research fellow at the Arizona Center for Mathematical Sciences, University of Arizona. He has a PhD in space physics from the University of Arizona. Contact him at armis@acms.arizona.edu.

Jerome V. Moloney is a professor of mathematics and optical sciences and a director of the Arizona Center for Mathematical Sciences at the University of Arizona. He has a PhD in chemical physics from the University of Western Ontario, Canada. Contact him at jml@acms.arizona.edu.

Masud Mansuripur is a professor of optical sciences and chair of the Optical Data Storage, Optical Sciences Center, at the University of Arizona. He has a PhD in electrical engineering from Stanford University. He is a fellow of the Optical Society of America. Contact him at masud@u.arizona.edu.

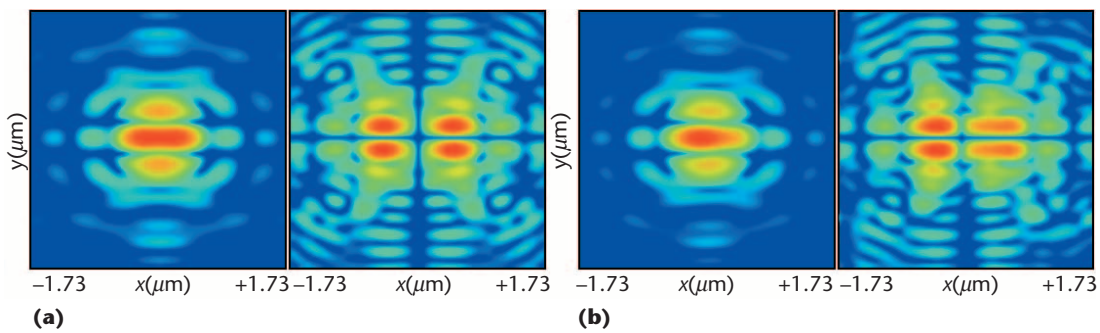

Figure 11. Plots of reflected log_intensity_3, from the groove with a circular recorded amorphous mark shifted along the groove by Δ = 0 (a, $P_x = 0.247$, $P_y = 0.0014$) and Δ = 180 nm (b, $P_x = 0.256$, $P_y = 0.0016$).